Mechanisms and kinetics of pore closure in thick aluminum plate

P. Gravier, F. Mas, A. Barthelemy, E. Boller, L. Salvo, Pierre Lhuissier

Graphical Abstract

Mechanisms and kinetics of pore closure in thick aluminum plate

P. Gravier, F. Mas, A. Barthelemy, E. Boller, L. Salvo, P. Lhuissier

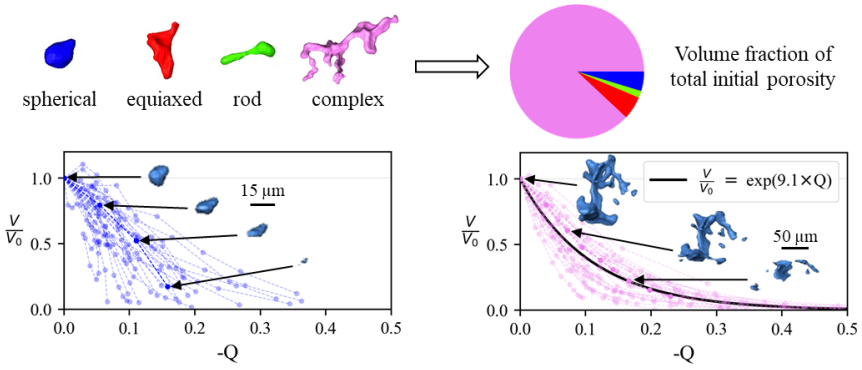

Mechanisms and kinetics of pore closure in thick aluminum plate

P. Gravier[a,b], F. Mas[b], A. Barthelemy[b], E. Boller[c], L. Salvo[a], P. Lhuissier[a,*]

[a] *Université Grenoble Alpes, CNRS UMR5266, Grenoble INP, Laboratoire SIMaP, 38000 Grenoble, France*
[b] *C-TEC Constellium Technology Center, Centr'Alp 725, rue A. Bergès CS10027, F-38341 Voreppe, France*
[c] *ESRF-The European Synchrotron, CS40220, 38043, Grenoble Cedex 9, France*

Abstract

Interrupted in situ tests at high temperature characterized with X-ray microtomography were employed to study porosity evolution under loading conditions representative of aluminum hot rolling. Coupling digital volume correlation and simulations, it is possible to access, for each pore, its morphological evolution, and the mechanical fields it experienced. The closure kinetics of hundreds of pores were studied, which is described as the pore volume as a function of the hydrostatic integration. Closure kinetics are a function of the shape of the pore. Focus is put on pores with a complex shape which are more detrimental to mechanical properties. Their closure kinetics are exponential due to the pore fragmentation during closure. The closure of complex pores is fostered by an initial orientation perpendicular to the loading direction and a low initial fragmentation. Based on the closure kinetics of 243 complex pores, a new pore closure model is proposed.

Keywords: Aluminum, Porosity, Closure kinetics, In situ X-ray microtomography, Pore closure model

*Corresponding author
Email address: pierre.lhuissier@simap.grenoble-inp.fr (P. Lhuissier)

1. Introduction

Thick aluminum plate is widely used in aerospace applications to machine structural aircraft elements. During casting, porosity appears in the ingot due to the higher density of solid aluminum and the lower hydrogen solubility in solid aluminum compared to liquid aluminum. Pores must be closed during the transformation because their presence in the final product would significantly decrease the mechanical properties of the material. The fatigue life of the material is reduced (Couper et al., 1990) as well as the ductility and tensile strength (Wu et al., 2012). Hot rolling is the processing step which enables to close the pores in these thick plates.

Park and Yang (1996) demonstrated that pore closure occurs in two steps. First morphology and topology of the pore evolve, along with the pore volume decrease. Then, the internal surfaces of the pore weld together during bounding. In the following, we will only focus on the first step also called mechanical closure by Saby et al. (2015b). The present work aims at a better understanding of pore closure mechanisms and at providing a better description of pore volume evolution during pore closure.

From the literature, we can report that mechanical fields expressed through the triaxiality and cumulated strain play a major role in pore closure, they were used by Gurson (1977), Duva and Hutchinson (1984), Zhang et al. (2009) and Saby et al. (2015a). Besides, closure also depends on pore shape and orientation, as shown by Saby et al. (2015a) who developed a closure model for ellipsoidal pores taking into account the orientation and the shape of the pore. Llanos et al. (2008) observed that natural holes are harder to close than artificial drilled holes. Nevertheless, most of the experiments and numerical simulations are conducted on simple pore geometries (spherical or ellipsoidal) whereas real casting pores can be branched and tortuous. The present paper investigates, using in situ X-ray microtomography, the closure of real pores experiencing

loading paths representative of hot rolling.

2. Experimental methods

The experimental methods are detailed in Gravier et al. (under revision - PROTEC-D-21-02245). In summary, in situ mechanical tests at high temperature characterized by X-ray microtomography are performed to mimic hot rolling loading and observe porosity evolution during deformation. Tests are performed in a synchrotron (ESRF-ID19, Grenoble, France), providing volumes with a voxel size of 2.44 μm where the whole sample and pores are visible.

This method provides 3D images of samples. Post treatment based on image processing, Digital Volume Correlation (DVC) and simulations allows the morphological evolution of tens of pores in each sample to be obtained as well as the local loading paths they experienced.

For the following study of pore closure, we will use data provided by the compression of cylindrical samples. Their dimensions are about 2 mm in diameter and 2 mm in height, they are made of 2XXX series alloy in which porosity was purposely increased. The samples are extracted in casting ingot after homogenization. The microstructure is typically made of equiaxed grains with an average grain size of 180 μm and a random texture. In these samples, the volume fraction of porosity ranges between 2.5×10^{-4} and 8.5×10^{-4}. The volume fraction of intermetallics is around 3×10^{-3}. For the compression, loading is applied along the height of the samples (which will be the vertical direction on the following figures). Five samples are compressed at 480 °C with a compression speed of 1000 $\mu m.s^{-1}$, we will refer to these conditions as standard conditions. Two different temperatures (455 and 520°C) and two lower compression speeds (100 and 500 $\mu m.s^{-1}$) are also tested.

3. Porosity description

Each sample typically contains tens of pores (Figure 1.a). However, because of the resolution of tomography, the precise number of pores is difficult to determine unambiguously, as apparently separate pores may in reality be connected by unresolved thin ramifications. Also, some of the pores are close to each other and may interact during deformation (Figure 1.b). In order to describe precisely the tomographic observations, we will use here the concepts of clusters and subpores. Subpores are all the pores that are separate from one another after thresholding (Figure 1.c). When these subpores are less than 50 µm apart (or 20 voxel surface to surface distance), they belong to the same cluster (Figure 1.d). The distance of 50 µm was chosen such that big clusters do not merge. It should be noted that the standardized dye penetrant inspection, used to validate industrial plate production, quantifies objects similar to these clusters: Kishimoto et al. (1989) demonstrated that if pores are close to each other, they can be considered as the same pore. The porosity is composed by the sum of all the clusters contained inside the sample. If we are able to predict the volume evolution of each single cluster, we are then able to compute the volume evolution of porosity.

A cluster can be composed of one or more subpores. A cluster's fragmentation is defined as the number of subpores it contains. As the tomographic resolution might be too coarse to image thin ramifications between subpores, fragmentation tends to be overestimated. Nevertheless, subpores that appear separate due to the resolution limitations but are actually connected will be contained within the same cluster. Thus, in this paper the volume evolution of pores will be investigated at the scale of clusters.

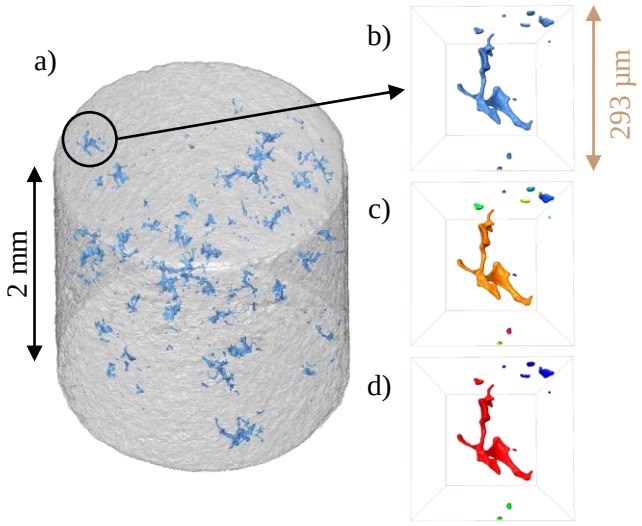

Figure 1: a) 3D rendering of pores (in blue) within a cylindrical sample. b) Zoom on pores. c) Pores colored by subpores: each individual pore has a different color. d) Pores colored by clusters: pores less than 50µm apart belong to the same cluster and have the same color.

The pores present in the samples have various shapes. They appear at solidification due to two concurrent mechanisms as reported by Dantzig and Rappaz (2016). On the one hand, the lack of mass feeding to compensate for the volumetric shrinkage causes the formation of pores in the interdendritic region. These pores are branched and tortuous. On the other hand, the lower hydrogen solubility in solid aluminum compared to liquid aluminum results in the liquid enrichment in gas. The gas is rejected under the shape of bubbles forming spherical pores. Shape has been reported to have a strong influence on pore closure. Llanos et al. (2008) observed differences between artificial and drilled pores, Chen et al. (2010) reported differences in the simulated closure of tetrahedral and spherical pores and Saby et al. (2015a) took into account

shape factors in the closure of ellipsoids. Based on these observations, pores are classified into 5 categories: spherical, equiaxed, rod, sheet and complex. The shape classification is adapted from the work of Fang et al. (2016) and is applied to subpores. Shapes are determined as a function of three parameters (Tab. 1): pore elongation E (Eq. 1), flatness F (Eq. 2) and complexity C (Eq. 3).

$$E = \frac{2a}{b+c} \tag{1}$$

$$F = \frac{b}{c} \tag{2}$$

Where $a > b > c$ are the semi-axes of the pore equivalent ellipsoid, namely the ellipsoid with the same inertia matrix (see Figure 2).

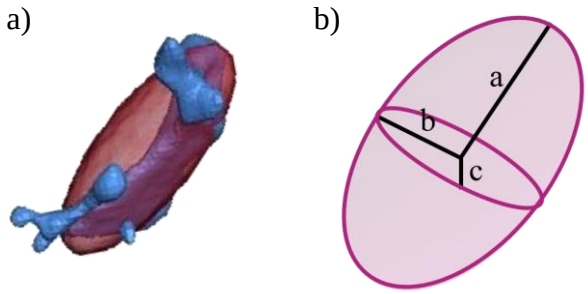

Figure 2: a) 3D rendering of a pore (in blue) with its equivalent ellipsoid (in red) that have the same inertia matrix as the pore. b) Semi-axes of the equivalent ellipsoid, $a > b > c$.

$$C = \frac{1}{s} = \frac{1}{6V}\sqrt{\frac{A^3}{\pi}} \tag{3}$$

s is the sphericity defined as the ratio of the pore volume V over the volume of a sphere having the same surface area A. For a sphere $s = 1$, $s < 1$ otherwise.

Shape	E	F	C	Color code
Spherical	/	/	$C \leq 1.5$	blue
Equiaxed	< 4	< 5	$1.5 < C < 2.5$	red
Rod	≥ 4	< 5	$1.5 < C < 2.5$	green
Sheet	/	≥ 5	$1.5 < C < 2.5$	yellow
Complex	/	/	$C \geq 2.5$	pink

Table 1: Shape classification

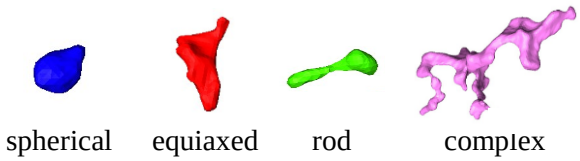

Figure 3: Examples of 3D views of different pore shapes according to the classification defined in table 1. Note that according to this classification, spherical pores can have protrusions and equiaxed pores can have small branches.

Examples of subpores of each category are shown in Figure 3, no flat subpores corresponding to sheet category were found in the present studied samples. Color code defined in table 1 will be used in all figures when shape classification is involved. In the following, simple shapes will refer to shapes with a low complexity, namely spherical, equiaxed and rod shapes.

A shape is also attributed to each cluster. Given that a cluster can be composed of subpores with different shapes, the cluster shape is the shape which is the most represented in volume fraction.

The size of a subpore (or a cluster) will be described with the equivalent diameter D_{eq} which is the diameter of a sphere having the same volume V as the subpore (or cluster) (Equation 4).

$$D_{eq} = 2\left(\frac{3}{4\pi}V\right)^{\frac{1}{3}} \tag{4}$$

Finally, orientation is defined at the cluster scale using equivalent ellipsoid. The semi-axes of the ellipsoid ($r_1 > r_2 > r_3$) and their respective direction ($\overrightarrow{u_1}$,$\overrightarrow{u_2}$,$\overrightarrow{u_3}$) are computed from the inertia matrix of the cluster. Cluster orientation is the value of the angle between the direction of the major axis ($\overrightarrow{u_1}$) and the direction of macroscopic loading (vertical direction in the following figures).

4. Results and discussion

4.1. Shape and size of subpores in the initial state

Figure 4 shows the distribution of subpores as a function of their shape and their equivalent diameter. These are subpores present in the initial state in a given sample.

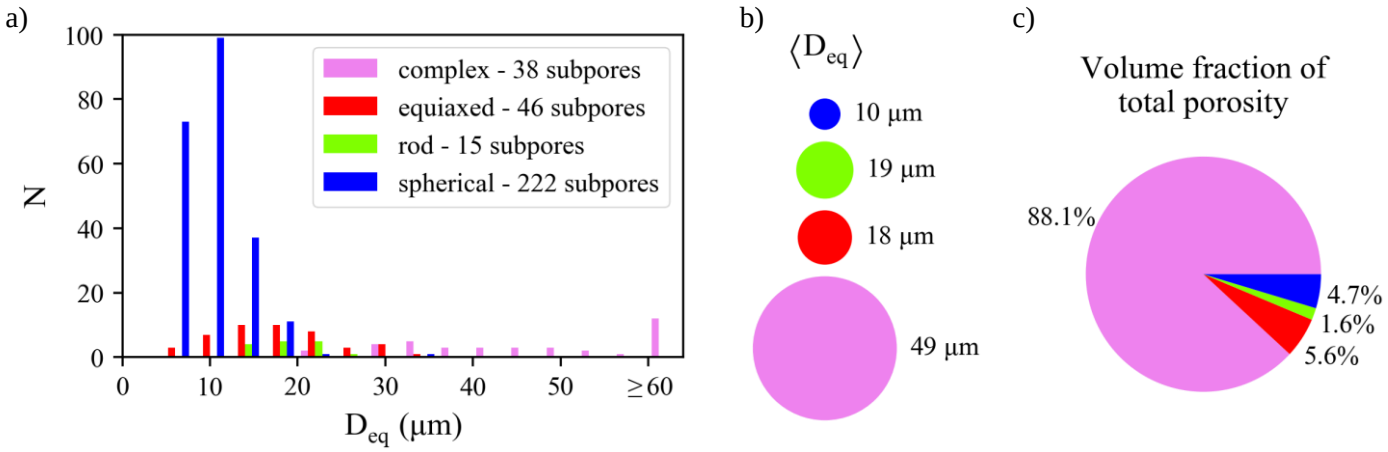

Figure 4: Shape and size of subpores in the initial state for a given sample. a) Distribution of subpores as a function of their equivalent diameter and shape. b) Mean equivalent diameter of subpores per shape. c) Contribution of each shape on the total volume of porosity.

The biggest subpores are complex with an equivalent diameter globally over 20 μm (Figure 4.a), their average equivalent diameter is 49 µm (Figure 4.b).

Conversely, spherical subpores have a low equivalent diameter, generally under 20 μm (Figure 4.a). Note that no quantification of subpores was performed below a volume of 8 voxels to avoid artifacts due to image noise. At such a small volume (equivalent diameter of 6 μm), the distribution of voxels cannot form a complex shape, so small pores are more likely to appear spherical due to resolution limits. Equiaxed and rod subpores have intermediate sizes between those of spherical and complex subpores.

Even if spherical subpores are more numerous, complex subpores represent 88% of the total volume of porosity (Figure 4.c). Complex subpores represent most of the porosity. Furthermore, they are the biggest, making them potentially more harmful for mechanical properties. Couper et al. (1990) demonstrated that the fatigue life of the material is increased when pores are smaller. Based on these observations, the description of closure of complex clusters is a key issue.

4.2. Shape evolution of subpores during closure

During the compression of cylindrical samples, porosity decreases because of negative triaxiality in most of the volume and large plastic deformation. Due to friction with the dies, the deformation is not homogeneous in the sample: zones close to the dies hardly deform and the sample takes a barrel shape. It induces tensile stresses on the sides of the samples which prevent pore closure and even lead to pore growth or pore nucleation. Therefore, at the end of the compression, pores are closed at the center of the sample and some pores may remain on the edges or may even appear in the last step of compression. Figure 5 shows the 3D rendering of pores within a cylindrical sample during compression. Most of the pores initially present are closed after a reduction of 59 %. Few pores are still present at the end of the test: on the edges due to tension and close to the top and bottom surface due to low deformation in these regions.

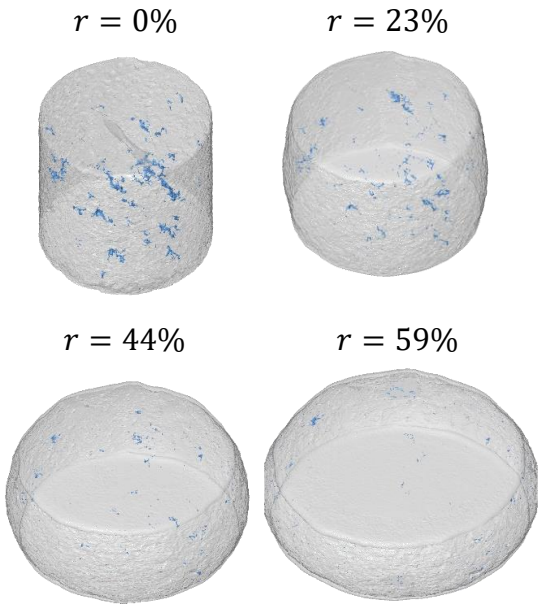

Figure 5: 3D rendering of pores (in blue) within a cylindrical sample during its compression.

At every compression step, a shape was assigned to each subpore. This shape is independent of the subpore history meaning that a subpore can have different shapes at different deformation steps. For each shape category, average equivalent diameter and number of subpores are plotted in Figures 6.a. and b.

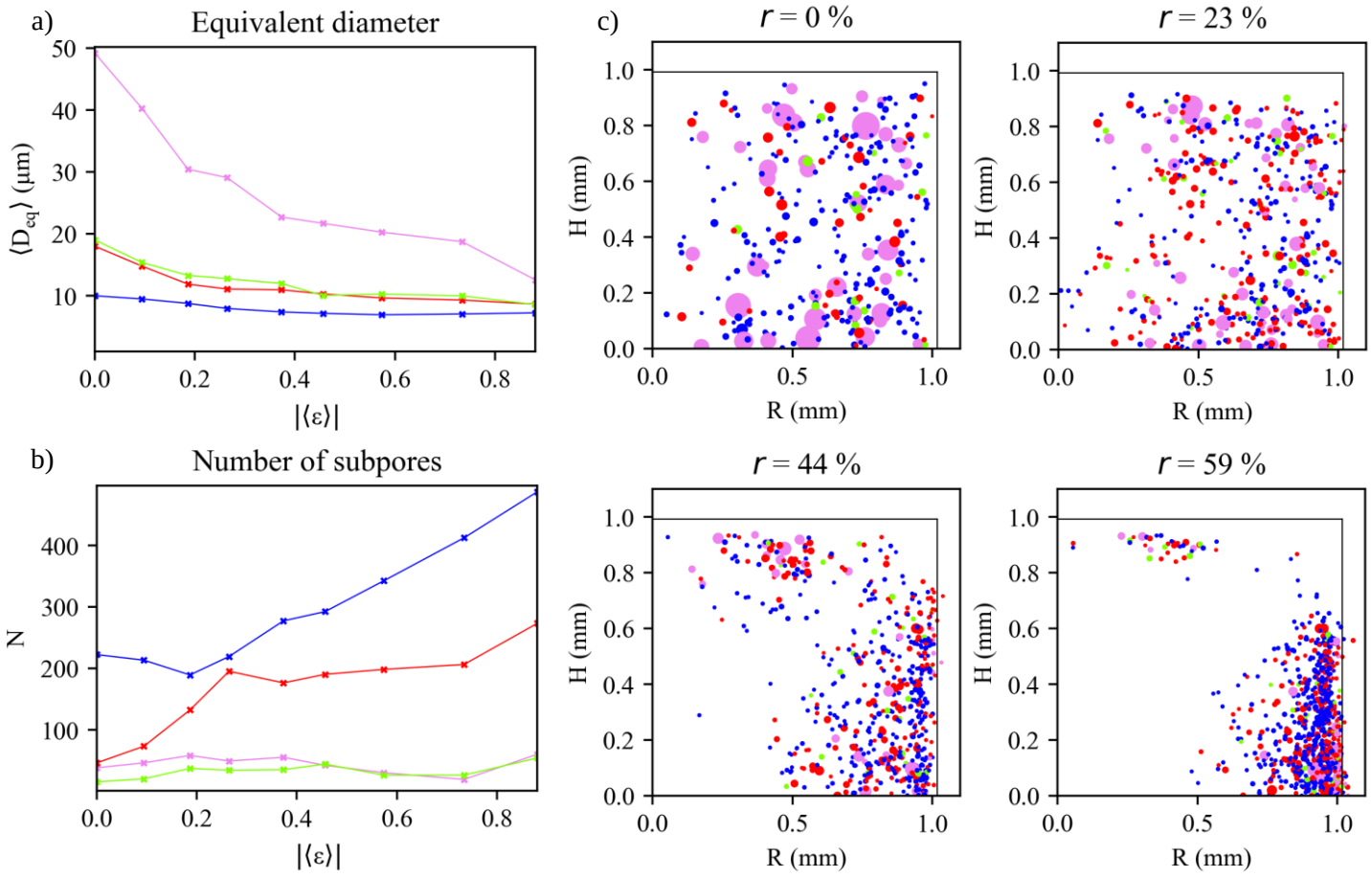

Figure 6: Evolution in size and number of subpores during compression depending on their shape. a) Evolution of the average equivalent diameter per shape. b) Evolution of the number of subpores per shape. c) Subpores position, size and shape in the axisymmetric projection. Position is represented in the initial state using the estimated initial position given by DVC. The deformation of the sample is not represented to ease the visualization of tracking.

155 The number of subpores can increase due to fragmentation or nucleation, or

decrease due to total closure or coalescence. The number of complex subpores remains constant during the early stage of deformation but their average equivalent diameter decreases sharply. This can be explained by the fragmentation of complex pores into a smaller complex pore and other simpler shapes such as equiaxed pores. The increase in the number of equiaxed pores supports this argument. On the other hand, the number of spherical pores decreases at the beginning of compression meaning that there is more spherical pores that close than spherical pores that appear due to fragmentation. After a strain of 0.3, the number of equiaxed pores reaches a plateau: there is an equilibrium between the creation of equiaxed pores from the fragmentation of bigger complex pores and the fragmentation of equiaxed pores into spherical pores.

This fragmentation of large complex subpores to smaller subpores of simpler shapes is visible on Figure 6.c. Subpores are projected on the axisymmetric plane. For each deformation step, subpore position is represented in the initial state using the estimated initial position given by DVC. Thus, deformation of the sample is not represented. Using initial configuration representation helps subpore tracking: if subpores are located at the same position at different deformation steps, they are likely to be the same subpore. Subpores are represented by disks of equivalent diameter (meaning that the disk diameter is equal to the subpore equivalent diameter). Disk color describes the associated subpore shape. Complex subpores decrease in size and split into new equiaxed, rod or spherical subpores. Equiaxed subpores become spherical and finally close. This Figure also shows the nucleation of small spherical subpores close to the edges. It is correlated with the final increase in number of spherical subpores. Finally, subpores located near the dies do not close because of low strain in this zone.

4.3. Morphology evolution of clusters during closure

The evolution of individual cluster morphology has been characterized by the cluster fragmentation and the shape evolution of the subpores in the cluster.

For spherical clusters, there is no fragmentation. Cluster are generally com-

posed of a single subpore. The subpore closes progressively, remaining spherical or sometimes becoming equiaxed due to flattening. The final description of spherical pore closure is limited by the resolution of tomography. In contrast, complex clusters are initially composed of several subpores. They are generally made of a central big complex subpore surrounded by smaller subpores. It is possible that these subpores actually connect but that the resolution limit does not enable to see the connection. An example is given on Figure 7. In the present case, the cluster is initially composed of 2 complex subpores with the biggest at the center. They are surrounded by 8 smaller subpores (rod, equiaxed or spherical). The figure describes the evolution of the composition of the cluster during the test. After the first compression step, the smallest complex subpore (at the upper left) fragments into a rod and a spherical subpores. The main complex subpore fragments also but generates only small subpores with simple shapes (from scan 1 to 3). Most of the volume remains in the complex subpore until scan 4. From then on, the big complex subpore fragments into 4 smaller complex subpores of similar volumes and other simple subpores. From scan 6, these complex subpores evolve to simpler shapes and finally close. The overall number of subpores first increases, owing to fragmentation and then decreases due to pore closure.

3D renderings also show that when the cluster has lost most of its volume, its dimension is still large. At scan 4, only 24% of the pore volume remains whereas its dimension perpendicular to the compression direction seems to remain unchanged. The cluster can still be detrimental for mechanical properties even when it reaches a low relative volume because, as observed by Murakami and Endo (1994), the pore has a crack shape. Therefore, it is necessary to describe finely the final closure of clusters up to a very small remaining volume.

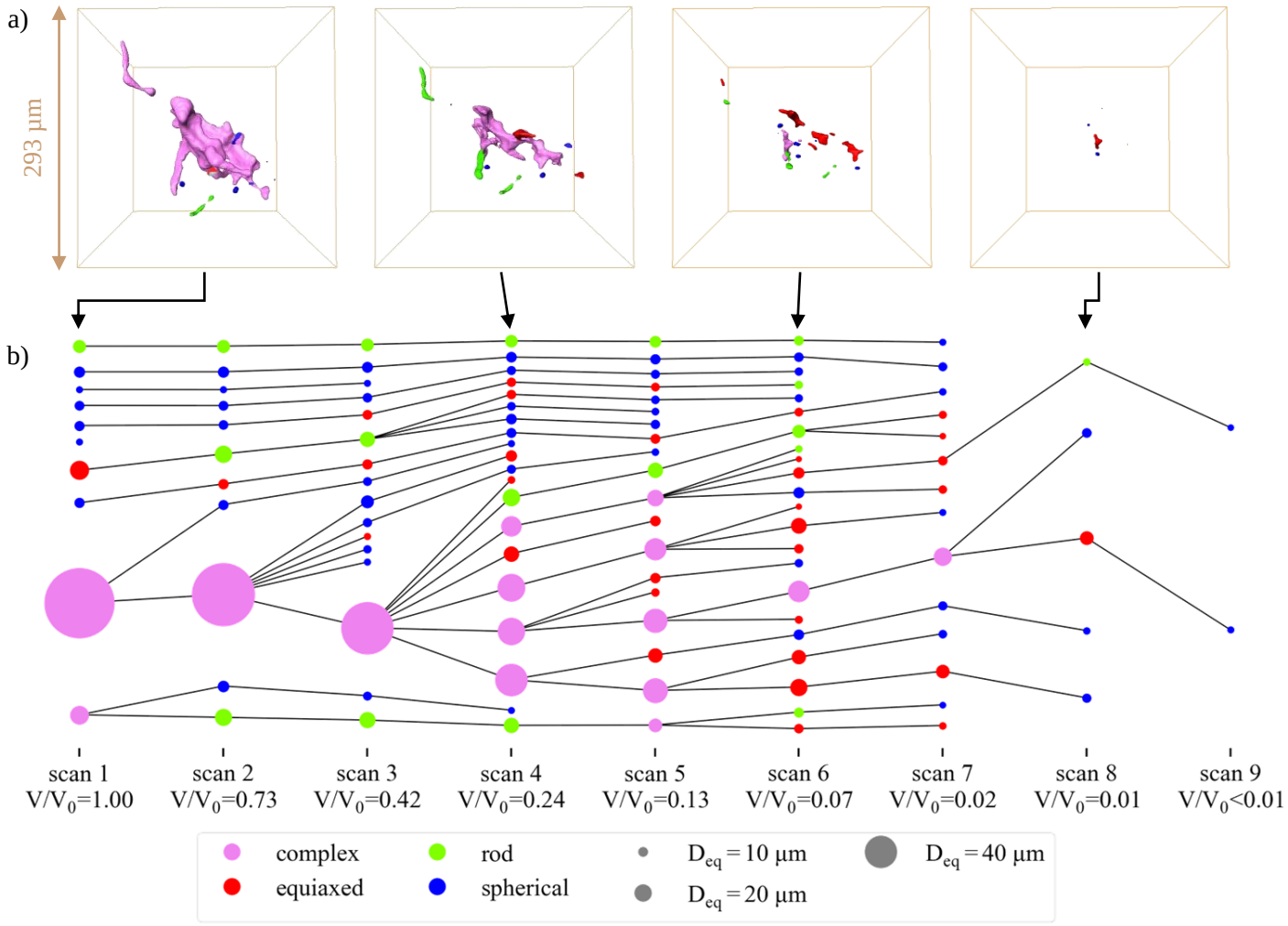

Figure 7: Fragmentation of a complex cluster during closure. a) 3D rendering of the cluster at different compression steps (loading was applied in the vertical direction). b) Schematic representation of the subpores composing the cluster.

4.4. Closure kinetics

According to literature, triaxiality T_X and cumulated strain $\bar{\varepsilon}$ are the two main parameters controlling pore closure. The hydrostatic integration Q (Equa-

tion 5) proposed by Tanaka et al. (1987) combines these parameters. Qualitatively, pore volume evolution correlates well with Q. Pore closure kinetics will be described by the evolution of the volume of pore clusters as a function of the hydrostatic integration Q.

$$Q(\bar{\varepsilon}) = \int_0^{\bar{\varepsilon}} T_X(\bar{\varepsilon}) d\bar{\varepsilon} = \langle T_X \rangle \, \bar{\varepsilon} \tag{5}$$

Recent pore closure models developed by Chbihi et al. (2017), Zhang et al. (2020), Wang and Dong (2020) take into account the Lode parameter μ in addition to the triaxiality. The influence of the Lode parameter affects the evolution of the pore volume when the traixiality is close to zero. In the present study, $\langle T_X \rangle \leq -0.1$ and $0 \leq \mu \leq 1$. Wang and Dong (2020) found that for a given pore at $\langle T_X \rangle = -0.3$, the closure strain is 0.55 for $\langle \mu \rangle = 1$ and it is 0.75 for $\langle \mu \rangle = 0$. On the other hand, Saby et al. (2015a) observed that the closure strain varies by twice on ellipsoids when different orientations or shape factors are considered. In the present case of real casting pores, the effect of the Lode parameter will be neglected compared to the effect of morphology. Thus we will not take the Lode parameter into account to study closure kinetics. The pores studied here experience stress states representative of the center of the plate or close to the rolls during rolling. They are not representative of the edges of the plate where the triaxiality is positive or close to zero. More details on the reproduction of stress states are given in Gravier et al. (under revision - PROTEC-D-21-02245).

Closure kinetics are studied observing clusters in compressive zones of cylindrical samples deformed by compression. Closure kinetics of all the clusters in a given cylindrical sample are presented on Figure 8.a. As hydrostatic integration is negative and decreases along deformation, $-Q$ is used for the X-axis. Only points with non-zero volume are represented on these graphs. When volume is equal to zero it is not possible to determine if clusters are really closed or if they are no longer detected (lost during tracking or volume lower than detection limit of 8 voxels). In the following, clusters with an initial volume of less than

40 voxels (= 581 μm^3) were not considered because their volume is lower than 8 voxels when they reach 20% of their initial volume. For such small clusters, final closure cannot be studied.

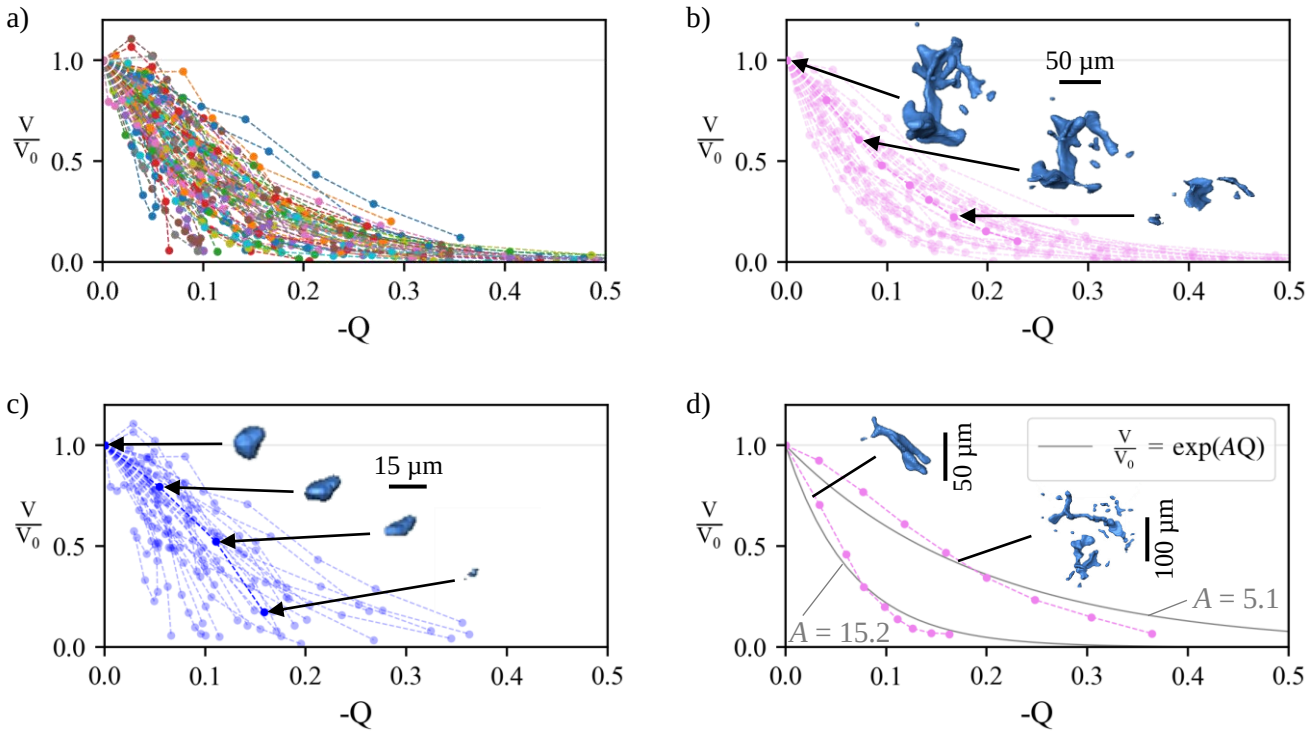

Figure 8: Cluster closure kinetics in a sample. a) All clusters. b) All complex clusters with an example of morphology evolution. c) All spherical clusters with an example of morphology evolution. d) Example of the exponential fit on two complex clusters and 3D rendering of their initial shape.

Saby et al. (2015b) noted that pores were closed for $Q < -0.2$ for STB model. For Nakasaki et al. (2006), closure is reached when $Q < -0.23$. Kakimoto et al. (2010) observed closure for $Q < -0.21$. Nevertheless, in the present case, many clusters are still open for such values. This difference can be explained by the

fact that in the cited papers, pores are either spherical or cylindrical whereas real pores are considered in the present study, including complex shapes.

A large scatter in closure kinetics is observed. The influence of morphological parameters is investigated to determine whether they can explain this scatter.

First, shape has an influence on pore closure kinetics. Figure 8.b presents the closure kinetic of all complex clusters in a given sample. Figure 8.c presents the closure kinetics of spherical clusters in the same sample. As spherical clusters are smaller than complex clusters, the relative uncertainty in their volume measurement is higher. Only their initial closure can be described as they reach the minimal volume of 8 voxels for a higher normalized volume. For complex clusters, the volume decreases exponentially with Q whereas spherical clusters closure is more linear or quadratic with Q. This difference could be explained by the fact that complex subpores fragment whereas spherical subpores remain a unique entity during closure. Saby (2013) reported that fragmentation slows down pore closure. In our case, fragmentation happens even in the early stage of closure (Figure 7) when closure rate is still high and it rather seems that the kinetics slow down when the biggest subpore of the cluster fragments in several subpores of similar sizes.

An accurate description of the volume evolution of complex clusters is more important than for spherical clusters since complex clusters are the largest and the most detrimental for mechanical properties. We propose to describe complex cluster closure kinetics using an exponential relation with the hydrostatic integration. For each complex cluster, the following formula was fitted, determining an exponential coefficient A per cluster.

$$\frac{V}{V_0} = \exp\left(AQ\right) \tag{6}$$

Q being negative in compression and for positive values of A, this curve decreases with cumulated strain. Figure 8.d shows the fitting curve for two

complex clusters. The higher the value of A, the faster the closure kinetics of the pore.

The proposed fit can be expressed by the following derivative form:

$$\frac{\dot{V}}{V} = A\, T_X\, \dot{\bar{\varepsilon}} \tag{7}$$

It is the same expression as the analytical volume evolution of a spherical pore in a linear viscous matrix calculated by Budiansky et al. Budiansky et al. (1982) where $A = 9/4$.

The fit proposed here tends to slightly overestimate initial closure and underestimate final closure but enables cluster closure ability to be easily sorted. The exponential coefficient is determined for all complex pores in the 9 cylinder samples. If the coefficient of determination r^2 is lower than 0.95, the pore is not taken into account. Such low coefficient of determination occurs for pores that are located in the zone of positive triaxiality or close to it. When triaxiality becomes positive, the hydrostatic integration which was decreasing starts to increase whereas pore volume continues to decrease before increasing. Misfits also result from low negative triaxiality. In that case, cluster volume keeps decreasing whereas hydrostatic integration decreases slower due to low negative triaxiality. It results in a too high negative slope compared to those of the exponential formula. These observations show the limitation of hydrostatic integration in the description of loading path.

In total 243 exponential coefficients A are fitted on closure kinetics of real complex clusters. Distribution of all the values obtained is presented on Figure 9.a.

Different parameters are tested to draw possible correlations between the exponential coefficients of a cluster and morphological and mechanical parameters. Some results are presented on Figures 9.b-d, all coefficients fitted for complex clusters in cylindrical compressed samples are gathered on this figure.

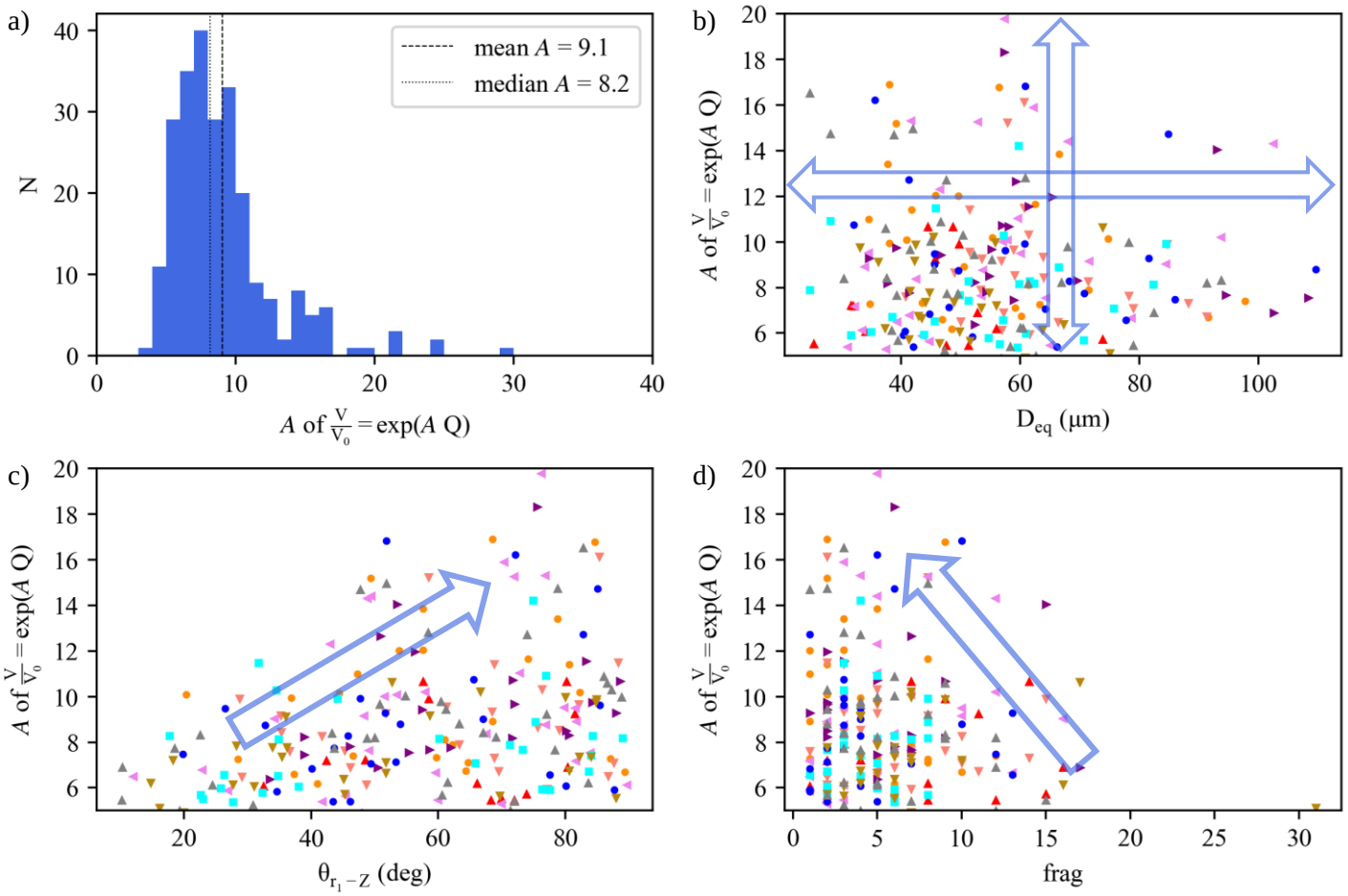

Figure 9: Study of the exponential coefficient A. a) Distribution of the values of A fitted on 243 closure kinetics of complex clusters. b-c) Dependency of exponential coefficient to several morphological parameters: equivalent diameter (b), orientation (c) and initial fragmentation (d).

The following observations can be made:

- A correlation between A and the equivalent diameter D_{eq} is not obvious

and thus, in the range of volume tested, pore closure does not depend on pore size. This observation is consistent with results of Saby (2013) and Chen and Lin (2013).

- Higher values of A are reached for clusters with a low initial fragmentation. In this case, interaction between individual subpores in a cluster would not be beneficial for closure. This is consistent with the results of Saby (2013) who observed that fragmentation slows down the closure kinetics.

- A reaches the highest values for clusters oriented perpendicularly to the deformation direction. This result is consistent with those of Saby (2013) where faster closure was observed for ellipsoids compressed along their smallest semi-axis (so compression direction forms an angle of 90°with the longest semi-axis). It is also consistent with the model of Feng and Cui (2015) which predicts faster closure for ellipsoids that have a low dimension in the compression direction. The orientation effect is accentuated by large aspect ratios (r_1/r_3). Here, only orientation is taken into account and not the ellipsoid aspect ratio. Thus, pores with low aspect ratio can be oriented perpendicularly to the compression and result in a low A value. Note that the notions of orientation and aspect ratio are more difficult to define for a real tortuous pore than for an ellipsoid. If the pore is branched, with arms in different directions, global orientation of the pore does not faithfully represent the different arms. It would be more relevant to adopt a more local description of the pore orientation.

As a conclusion, complex cluster closure kinetics are mostly influenced by the initial fragmentation of clusters and their orientations. It is difficult to determine the initial fragmentation and orientation of pores in an industrial plate prior to rolling. Thus, we propose a new closure model expressed by Equation 6 with a fixed value of $A = 9.1$ for all clusters. This phenomenological description represents the average closure behavior of studied complex clusters and captures the closure kinetics induced by fragmentation.

4.5. Effects of temperature and compression speed on closure kinetics

The previous results show data acquired during the compression of samples at different temperatures (455, 480 and 520°C) and speeds (100, 500 and 1000 $\mu m.s^{-1}$). FEM simulations have shown that the local loading paths, described by the evolution of stress triaxiality as a function of the cumulated strain, are not influenced by the temperature or speed Gravier et al. (under revision - PROTEC-D-21-02245). Thus, closure kinetics were considered independently of the compression conditions.

Figure 10 shows the distribution, under the shape of a boxplot, of the exponential coefficients in each studied sample (ends of the whiskers correspond to the largest points that fall within a distance of less than 1.5 times the interquartile range over the third quartile and under the first quartile). If the experimental conditions used to test a sample act in favor of pore closure, the distribution would be shifted toward higher A values. The figure shows that discrepancies between standard conditions and tests with different temperatures and speeds are less significant than discrepancies between samples tested with same standard conditions. It means that temperature and compression speed have a second order influence on pore closure compared to cluster morphology such as orientation or fragmentation.

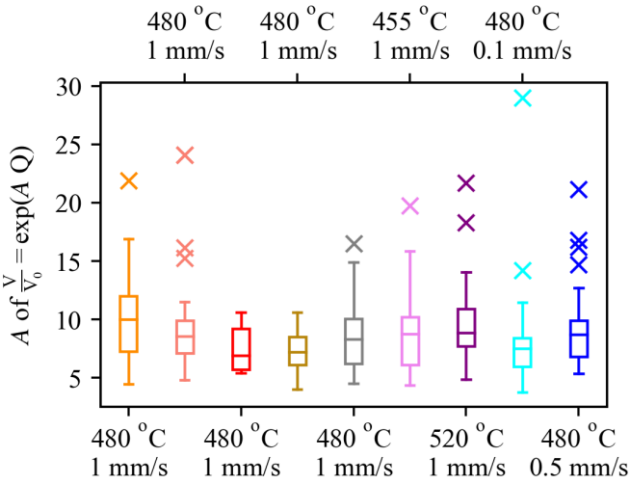

Figure 10: Boxplots of the distribution of exponential coefficient for the different samples.

5. Conclusions

In this work we were able to study porosity closure based on the observation of pores during their deformation using X-ray microtomography. These interrupted in situ tests were performed under conditions representative of hot rolling and the closure of several hundreds of real pores was followed. Pores were studied at two scales (subpores and clusters) and as a function of their shape (spherical, rod, equiaxed and complex). Based on this work, the following conclusions can be drawn:

- Complex clusters are bigger in size and represent the largest part of the porosity compared to pores with other shapes. The accuracy of the overall porosity prediction is mainly linked to the ability to properly describe complex subpores closure.

- During closure, complex subpores fragment into smaller subpores with simpler shapes.

- Closure kinetics strongly depend on cluster shape. Closure kinetics of complex clusters can be approximated by an exponential function of the hydrostatic integration whereas a linear or quadratic dependency on the hydrostatic integration is more suitable in the case of spherical clusters.

- For complex clusters, closure is influenced by the principal orientation and the initial fragmentation of the cluster. Clusters oriented perpendicularly to the compression direction and with low initial fragmentation are easier to close.

- Based on experimental data analysis, a new closure model is proposed: $V/V_0 = \exp(9.1\ Q)$. It only depends on the hydrostatic integration. It aims at properly describing complex pore closure up to relative volume far below 20% because pore dimensions are still large for such a remaining volume.

This study proposes a prediction model for pore closure by fitting experimental data. Nevertheless, many other models are available in the literature. Some of these models will be tested in a future paper. These models can be computed using the present data collected with X-ray microtomography and with the local mechanical fields provided by simulations.

Acknowledgments

The authors would like to thank the Association Nationale Recherche Technologie (ANRT) and Constellium Technology Center (C-TEC) for funding the project. The European Synchrotron Radiation Facility (ESRF) is gratefully acknowledged for offering beam-time associated to the MA3482 proposal. Thanks to Gary Admans for proofreading the article.

References

Budiansky B, Hutchinson J, Slutsky S. Void Growth and Collapse in Viscous Solids. Mechanics of Solids 1982;1(3):13–45.

Chbihi A, Bouchard PO, Bernacki M, Pino Muñoz D. Influence of Lode angle on modelling of void closure in hot metal forming processes. Finite Elements in Analysis and Design 2017;126(September 2016):13–25.

Chen Kb, Yang Y, Liu K, Shao G. Simulation of void defect evolvement during the forging of steel ingot. Advanced Materials Research 2010;97-101:3079–84.

Chen MS, Lin YC. Numerical simulation and experimental verification of void evolution inside large forgings during hot working. International Journal of Plasticity 2013;49:53–70.

Couper MJ, Neeson AE, Griffiths JR. Casting Defects and the Fatigue Behaviour of an Aluminium Casting Alloy. Fatigue & Fracture of Engineering Materials & Structures 1990;13(3):213–27.

Dantzig JA, Rappaz M. Solidification: Revised and Expanded. EPFL press, 2016.

Duva J, Hutchinson J. Constitutive potentials for dilutely nonlinear materials. Chemical Physics 1984;3(July):228–34.

Fang H, Versteylen CD, Zhang S, Yang Y, Cloetens P, Ngan-tillard D. Autonomous filling of creep cavities in Fe-Au alloys studied by synchrotron X-ray nano-tomography. Acta Materialia 2016;121:352–64.

Feng C, Cui Z. A 3-D model for void evolution in viscous materials under large compressive deformation. International Journal of Plasticity 2015;74:192–212.

Gravier P, Mas F, Barthelemy A, Boller E, Salvo L, Lhuissier P. Pore closure in thick aluminum plate: from industrial hot rolling to individual pore observation. Journal of Materials Processing Technology under revision - PROTEC-D-21-02245;.

Gurson AL. Continuum Theory of Ductile Rupture by Void Nucleation and Growth: Part I—Yield Criteria and Flow Rules for Porous Ductile Media. Journal of Engineering Materials and Technology 1977;99(1):2.

423 Kakimoto H, Arikawa T, Takahashi Y, Tanaka T, Imaida Y. Development of
424 forging process design to close internal voids. Journal of Materials Processing
425 Technology 2010;210(3):415–22.

426 Kishimoto K, Soboyejo WO, Knott JF, Smith RA. A numerical investigation of
427 the interaction and coalescence of twin coplanar semi-elliptical fatigue cracks.
428 International Journal of Fatigue 1989;11(2):91–6.

429 Llanos JM, Santisteban V, Demurger J. Improvement of central soundness in
430 long products from a through process control of solidification and reheating
431 and rolling. Technical Report; European Commission - Research Fund for
432 Coal and Steel; 2008.

433 Murakami Y, Endo M. Effects of defects, inclusions and inhomogeneities on
434 fatigue strength. International Journal of Fatigue 1994;16(3):163–82.

435 Nakasaki M, Takasu I, Utsunomiya H. Application of hydrostatic integration
436 parameter for free-forging and rolling. Journal of Materials Processing Tech-
437 nology 2006;177(1-3):521–4.

438 Park C, Yang D. A study of void crushing in large forgings I: Bonding mechanism
439 and estimation model for bonding efficiency. Journal of Materials Processing
440 Technology 1996;57(1-2):129–40.

441 Saby M. Compréhension et modélisation des mécanismes de refermeture de
442 porosité dans les procédés de mise en forme des métaux à chaud. Ph.D.
443 thesis; Mines ParisTech; 2013.

444 Saby M, Bouchard PO, Bernacki M. A geometry-dependent model for void
445 closure in hot metal forming. Finite Elements in Analysis and Design
446 2015a;105:63–78.

447 Saby M, Bouchard PO, Bernacki M. Void closure criteria for hot metal forming:
448 A review. Journal of Manufacturing Processes 2015b;19(2):239–50.

449 Tanaka M, Ono S, Tsuneno M. Factors contributing to crushing of voids during
450 forging. J Jpn Soc Technol Plast 1987;27(306):852–9.

451 Wang X, Dong X. A void evolution model accounting for stress triaxiality, Lode
452 parameter and effective strain for hot metal forming. International Journal
453 of Mechanical Sciences 2020;168(November 2019). doi:10.1016/j.ijmecsci.
454 2019.105309.

455 Wu X, Schlangen E, van der Zwaag S. Linking Porosity to Rolling Reduction
456 and Fatigue Lifetime of Hot Rolled AA7xxx Alloys by 3D X-Ray Computed
457 Tomography. Advanced Engineering Materials 2012;14(7):457–63.

458 Zhang Q, Niu L, Liang Z, Cao M, Zhou T. A porosity closure model consid-
459 ering stress triaxiality ratio and Lode stress parameter. Journal of Materials
460 Processing Technology 2020;286(May):116824.

461 Zhang XX, Cui ZS, Chen W, Li Y. A criterion for void closure in large ingots dur-
462 ing hot forging. Journal of Materials Processing Technology 2009;209(4):1950–
463 9.